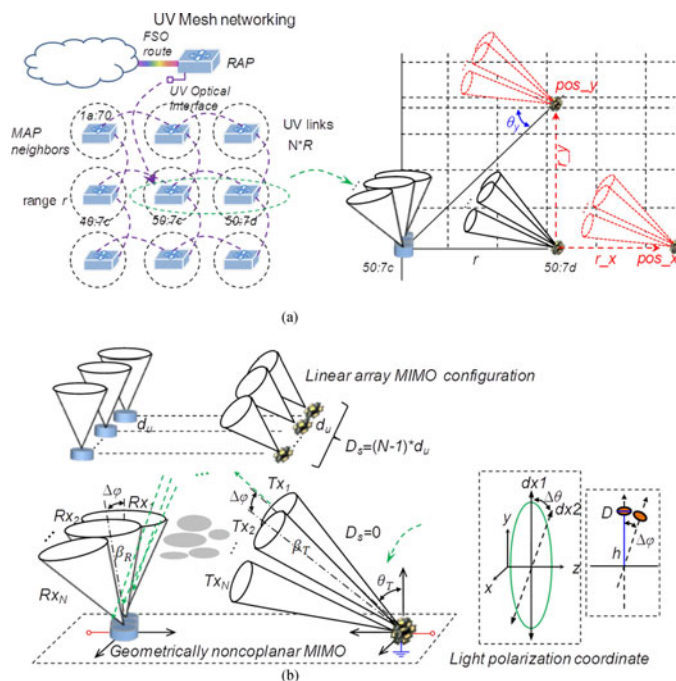# Noncoplanar Geometry for Mobile NLOS MIMO Ultraviolet Communication With Linear Complexity Signal Detection

Heng Qin
Yong Zuo
Feiyu Li
Risheng Cong
Lingchao Meng
Jian Wu

Noncoplanar Geometry for Mobile NLOS MIMO Ultraviolet Communication With Linear Complexity Signal Detection

Heng Qin, Yong Zuo, Feiyu Li, Risheng Cong, Lingchao Meng, and Jian Wu

State Key Laboratory of Information Photonics and Optical Communications, Beijing University of Posts and Telecommunications, Beijing 100876, China

Abstract: In this paper, we take a first step toward the mobile support for nonline-of-sight ultraviolet (UV) links by introducing a mesh UV network framework. Spatial multiplexing noncoplanar multiple-input-multiple-output (MIMO) UV system architecture is designed geometrically for the mobile mesh network to overcome the data rate bottleneck induced by scattered UV channel. Based on the MIMO UV channel characteristics, we further propose a modified sphere decoding (SD) method to accomplish MIMO signal detection in practical spatial correlated channels at a linear computational complexity. We evaluate mobile MIMO channel responses under various geometric parameters and the feasibility of this system geometry in 2×2 and 4×4 cases. Comparison of the bit error rates (BERs) between the modified SD, zero forcing, and SD is also done. Numerical results demonstrate that compared with the traditional linear array system structure, fully multiplexing is much easier via the noncoplanar MIMO geometry under very realistic parameters and the modified SD significantly improves the MIMO signal detection complexity with bit BER performance loss.

Index Terms: Non-line-of-sight ultraviolet communication, spatial multiplexing, modified SD detection.

1. Introduction

Increasing demand for wireless optical carrier is motivated by congestion in radio frequency spectrum [1]. Compared with conventional free space optical (FSO) transmission, non-line-of-sight (NLOS) links in ultraviolet (UV) spectral regions are proved to be feasible by atmospheric scattering, which offers two major advantages [2], [3]: 1) pointing and tracking between transmitter (Tx)/receiver (Rx) is relaxed; 2) solar-blind feature encourages a wider field of view (FOV) Rx. Thus, great opportunity on UV optical links is found in many potential communication scenarios [4], [5]. Recently, significant progress has been made on UV point-to-point links e.g., path loss model, modulation schemes, detector performance, system design [6]–[9] and networks e.g., connectivity issues, outage probability [10]–[12]. However in existing studies, the Tx/Rx nodes maintain a fixed position for both cases. A network model supporting mobile connecting links for NLOS UV communication is absent. in this paper, a mesh network framework is introduced on UV scattered channels

for the mobile demand owing to its scalability for wide coverage [13]. Channel mobility is defined by two directional elemental node movements in space.

For NLOS mobile UV connected networks, higher data rate is required technically as temporal dispersion by photon scattered propagation restricts the achievable channel bandwidth [14], [15]. Low-density-parity-check code (LDPC) has been investigated in [16] and our previous works [17] to improve the data rate. Nevertheless, higher spectral efficiency is still needed for UV channels because LDPC cannot offset the limited bandwidth. According to modern digital communication theory, multiple-input-multiple-output (MIMO) provides a chance of resolving this bottleneck [18]. But, previous studies on MIMO UV systems were mainly confined to spatial diversity at the Rx side [19]–[21]. Spatial multiplexing (SM) which offers capacity gains is paid scarce attentions.

Two key issues are associated with the multiplexing MIMO UV systems. Firstly, although the data rate is increased by more antennas, the BER of MIMO system becomes worse due to the inter-subchannel inference caused by spatial correlation [22]. The spacing of Rx with wide FOV could be relative too large considering the size of LED/PMT to guarantee an independent MIMO channel if traditional linearly distributed Tx/Rx arrays are implemented. Thus, a MIMO Tx/Rx design promising independent MIMO channels is necessary. Secondly, in realistic MIMO UV channels, inter-subchannel interference may exist due to partial spatial correlation. An efficient MIMO signal detection is also vital. In [23], zero forcing (ZF) is investigated in a 3×3 UV system. However, despite the calculation simplicity, the BER performance of ZF is highly dependent on the channel independence [24]. In contrast, the sphere decoding (SD) offers equal detection accuracy with the optimal maximum likelihood (ML) detection (exponential computational complexity) [25]. But the complexity of SD (polynomial computational complexity) still becomes very large when the problem dimension is high.

Specifically, inspired by the polarized light field coordinate [26], we geometrically design the noncoplanar MIMO UV Tx/Rx to produce spatial independent MIMO channels [27]. Large datasets of the mobile MIMO UV channel responses in 2×2 and 4×4 cases are collected into a three dimensional illustration to verify this system geometry. Furthermore, based on the MIMO UV channel characteristics, we modify the SD algorithm to achieve linear computational complexity. System BERs are exploited in 4×4 cases using the modified SD, ZF and SD method. Numerical results exhibit that fully multiplexing is enabled by this noncoplanar geometry at a lower cost than the linear array structure and the order of BER using the modified SD is consistent with the SD in realistic partial spatial correlated channels as well as in mobile scenarios.

The organization of this paper is as follows. The mobile mesh UV network and noncoplanar geometrical MIMO UV system are described in Section 2. Section 3 discusses the MMO UV channel characteristics and develops the modified SD algorithm. Comparison of the BER performance between the different system structures and MIMO detection methods are given. Some conclusions are drawn in Section 4.

2. Description of the System Framework

In this section, we will firstly give a brief description to the mobile mesh UV network and define the mobile feature of the Tx/Rx nodes. Then we demonstrate the geometrically noncoplanar MIMO UV system design and derive the MIMO UV channel response by this specific system structure in part 2.2. In part 2.3, numerical results of the MIMO UV channel responses are illustrated and the impacts of node movements are also discussed.

2.1 Mobile mesh UV Network Model

The hypothetical framework of the mesh UV network is depicted in Fig. 1(a). We apply the wireless mesh networking concept into the NLOS UV optical wireless scenario by substituting the backbone and wireless links with FSO route and UV links. The key network components of a simple UV mesh deployment shown in Fig. 1(a) are the following [29]: Router access point (RAP) – provides the
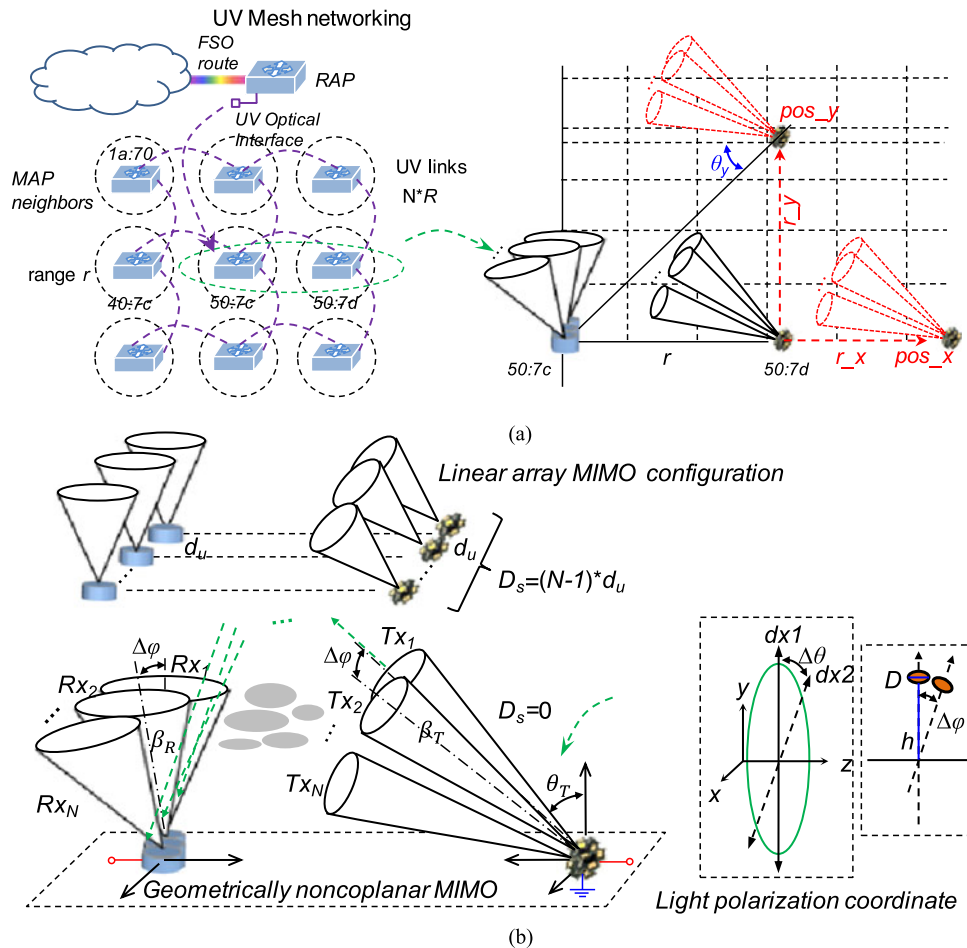
Fig. 1. (a) Illustration of the UV mesh network constructed with RAP and MAPs routed by backbone FSO links and hop-to-hop UV links. Nodes denoted by the MAC addresses are distributed in the mesh grid with coverage range of r. The right coordinate demonstrates the mobile UV channels featured by two elemental node movements on x axis and y axis of the mesh grid. R denotes the data rate upper bound of a single link. (b) Schematic drawing of the geometrically noncoplanar MIMO UV Tx/Rx design. $\triangle\varphi$ denotes the misalignment angle of the two adjacent cone axes. β_R is the FOV of the Rx, β_T is the beam divergence of the Tx, θ_T is the elevation angle of the Tx. A linear array Tx/Rx structure is also given where d_u is the Tx/Rx spacing and D_s is the Tx/Rx size quantized by $(N-1) * du$. $\triangle\theta$ denotes the included angle between dx1 and dx2, D is the diameter of a LED or PMT, h is the height of the optical antennas.

path home for the UV mesh to the core network by UV optical interfaces; A number of mesh access points (MAPs) – represent the distributed nodes in the UV mesh network. Each node is allocated with a 4-byte media access control (MAC) address e.g., 1a:70. The MAPs are connected with each other by a NLOS UV link within a coverage range of r. The mesh network structure provides scalability for short range UV transmission links, where multi-hop links between communication nodes at different geographical positions enlarge the network coverage.

Fig. 1(a) gives a demonstration of how the UV mesh setups and runs. The physical location of a RAP is on the edge of the mesh and a directional UV optical interface is used to establish a link into the mesh. The MAP actively solicits for neighbor APs, learns all of the available neighbors back to a RAP, determines which neighbor offers the best path, and then synchronizes with that neighbor. In the case above, MAP (50:7c) is the path for all traffic of the nodes. Ideally, the coverage from the RAP should be such that other MAPs, such as MAP (50:7d) for example, have a path back to the RAP, and traffic could be routed via MAP (50:7d) in case of a loss of signals to MAP (50:7c). If a

seamless coverage with approximately two to three hops is intended, you may have a typical mesh size radius of 200 m–300 m and nine MAP members considering the reliable range of a single hop NLOS UV link of around 100 m [10].

In the mesh UV network architecture, node movements in space can be decomposed into two elemental motions on the *x* axis and *y* axis termed as *x*-component and *y*-component as shown in the right coordinate of Fig. 1(a), where the Rx is assumed to fixed at the origin of and the Tx is initially located at distance *r* from the Rx, *r_x* denotes the path from the initial Tx position to position pos_x. Similarly, *r_y* denotes the path from the initial Tx position to position pos_y. *x*-component and *y*-component movement respectively describes the horizontal movement by the node relative to the direction from the Tx across the Rx and the vertical movement. Discussions on the mobile MIMO UV channel responses and the detection methods in the following sections are based on these two elemental movements. In the next part, we will see that *x*-component and *y*-component movements could bring different influences to the UV system geometric parameters.

2.2 Geometrically Noncoplanar MIMO UV System and Channel Model

Fig. 1(b) shows the noncoplanar MIMO UV system and the traditional linear array system structure including N Tx and N Rx. The Rx elevation angle θ_R is selected as 90° to make an omnidirectional receiving. The Tx elevation angle θ_T can be adjusted according to the link reliability which will be futher discussed in the following parts. As the path loss of NLOS UV links rises rapidly with the growing of θ_T, the transmission range is limiting considering a constant transmitted power and a target BER. Thus, the distance r between network nodes can be dynamically adjusted based on the scalability feature of the above mesh grid structure. As shown in Fig. 1(a), we can find that y-component movement changes the elevation angles of the Tx and Rx. We define the azimuth angle from the pos_y to the initial position by θ_y. When the node moves to pos_y, the Tx and Rx elevation angles will become to $\theta_T + \theta_y$ and 90°-θ_y. Oppositely, *x*-component movement only increases the channel path loss due to longer distance from the Rx.

As we know in classical optics, light is linearly polarized by passing it through a Polaroid. Suppose we have a second piece of Polaroid whose transmission axis makes an angle of $\Delta\theta$ with the first piece as shown in the light polarization coordinate of Fig. 1(b), where dx1 denotes the polarized direction of the first piece and d×2 denotes the polarization direction of the second piece. By the Malus law [26], intensity transmitted by both Polaroids can be expressed as $I(\Delta\theta) = E^2\cos^2(\Delta\theta)$, where E is the electric field amplitude. Similarly, in NLOS UV links, the misalign between the Tx beam axes and Rx FOV axes could also cause additional channel fading due to smaller scattered common volume [27]. Therefore, as shown in Fig. 1(b), the geometrically noncoplanar MIMO UV Rx/Tx design where all Tx or Rx are distributed on the polarization structured coordinate can enable spatial independent MIMO UV channels by the uncorrelated FOVs at different Rx. Let R denote the data rate of a single UV link. By this MIMO structure, the link data rate will be N-fold of R in N × N MIMO cases. For example, fourfold of R is specified in 4 × 4 cases.

Criterion 1 ($\Delta\varphi$): In the above MIMO configuration, an important problem needed to concern is the size of $\Delta\varphi$. The right parts of Fig. 1(b) show a practical system deployment, where, D is the diameter of a LED or PMT which is about 10 mm [2], the height of optical antennas h in an integrated circuit is supposed to be about 10 cm. Thus the minimum of $\Delta\varphi$ can be expressed as $2\tan^{-1}(D/h)$ according to the above coordinate. We also maintain a boundary of 60° to $\Delta\varphi$ for realistic convenience. Thus the range of $\Delta\varphi$ is given by [5°, 60°].

Theorem 1 (MIMO UV channel response): Considering the noncoplanar MIMO UV system, we derive the MIMO UV channel response model to detect the MIMO UV channel characteristics. Due to the short distance between network nodes, single scattered propagation model is assumed to depict the UV channel and extended to MIMO cases. UV photons from the Tx arrive at various Rx across different random paths at different times. Denote the time-varying channel impulse response between the *j*th Tx and the ith Rx as $h_{ij}(\tau, t)$. The composite MIMO channel response can be given

by a $N \times N$ matrix $\boldsymbol{H}(\tau, t)$ with [22]

$$H(\tau, t) = \begin{bmatrix} h_{11}(\tau, t) & h_{12}(\tau, t) & \cdots & h_{1N}(\tau, t) \\ h_{21}(\tau, t) & h_{22}(\tau, t) & \cdots & h_{2N}(\tau, t) \\ \vdots & \vdots & \ddots & \vdots \\ h_{N1}(\tau, t) & h_{N2}(\tau, t) & \cdots & h_{NN}(\tau, t) \end{bmatrix}. \tag{1}$$

For NLOS UV links, $h_{ij}(\tau, t)$ can be obtained by the Monte Carlo method through statistically counting the temporal distribution of numerical photons at the ith Rx transmitted from the jth Tx [6]

$$h_{ij}(t) = \sum_{l=1}^{L} \alpha_{ij}^{(l)} \delta(t - \tau_{ij}^{(l)}), \tag{2}$$

where L is the total number of the resolved scattered multipath, τ is the time delay of the lth resolved multipath at the ith Rx, α is the amplitude considering both the atmospheric attenuation and scattered propagation. Furthermore, given that $s_j(t)$ is launched from the jth Tx, the output at the ith Rx becomes $y_i(t) = h_{ij}(t) * s_j(t) + n_i(t)$, where $n_i(t)$ is the additive noise comprised by thermal noise and receiver amplified noise [15]. Then under the narrowband assumption, the reciprocal of the transit time $1/T_s$ is much smaller than the UV channel coherent bandwidth B_c, which permits the data rate upper bound [22]. Thus, the convolution in the above expression can be substituted by a multiplicative term $h_{ij} = \sum \alpha_{ij}^{(l)}$ which represents the average path loss (dB) from the jth Tx to the ith Rx [17]. Moreover, the geometrically symmetric MIMO structure depicted in Fig. 1(b) generates a numerically symmetric MIMO UV channel matrix. Finally, we can get a symmetric deterministic MIMO UV channel response matrix $\boldsymbol{H}$ expressed as follows

$$H = \begin{bmatrix} h_{11} & h_{12} & \cdots & h_{1N} \\ h_{12} & h_{22} & \cdots & h_{2N} \\ \vdots & \vdots & \ddots & \vdots \\ h_{1N} & h_{2N} & \cdots & h_{NN} \end{bmatrix}, \tag{3}$$

where $h_{11} = h_{22} = \cdots = h_{NN}$. $\boldsymbol{H}$ can be then reformed into a coefficient matrix normalized by h_{11}. Note that $h_{1N} < h_{1N-1} < \cdots < h_{12}$, which enables the independence between subchannel elements of $\boldsymbol{H}$. In addition, because of the uniform distribution of all the Tx/Rx, the ratio of each pairs $[h_{ki} h_{kj}] (k = 1, .., N) h_{ki}/h_{kj}$ is constant if i-j stays equal. For example, $h_{12}/h_{22} = h_{32}/h_{22}$ and $h_{24}/h_{44} = h_{13}/h_{33}$.

2.3 Numerical Results of the Mobile MIMO UV Channel Responses

In order to verify the independence of the symmetric MIMO UV channel and analyze the influences of the node movements on the MIMO UV channel. We firstly numerically simulate $\boldsymbol{H}$ in 2×2 cases and 4×4 cases under various $\Delta\varphi$ and θ_T. The results are plotted from a three dimensional view as shown in Fig. 2. In our simulations, the atmospheric parameter including the wavelength λ, absorption coefficient k_a, Rayleigh scattering coefficient k_r, Mie scattering coefficient k_m, atmospheric parameter γ, g, and f can be found in [6] and are also given in the caption of Fig. 2. β_T and β_R are chose as 15° and 40°.

The 2×2 channel response when distance $r = 30$ m is given in Fig. 2(a). From the results, we find that the amplitude of h_{12} decreases with $\Delta\varphi$ and θ_T. Besides, θ_T dominants the relationship of the subchannel elements against $\Delta\varphi$. h_{12} decreases faster when θ_T is smaller. Furthermore, h_{12} is almost 0 when $\Delta\varphi$ is up to 20° if θ_T is 30°. In this case, an identity channel matrix is resulted due to the symmetric channel structure, which helps build fully independent channel. Similar outcomes appear in 4×4 cases. Fig. 2(b) shows the 4×4 channel response when $r = 100$ m. It is observed
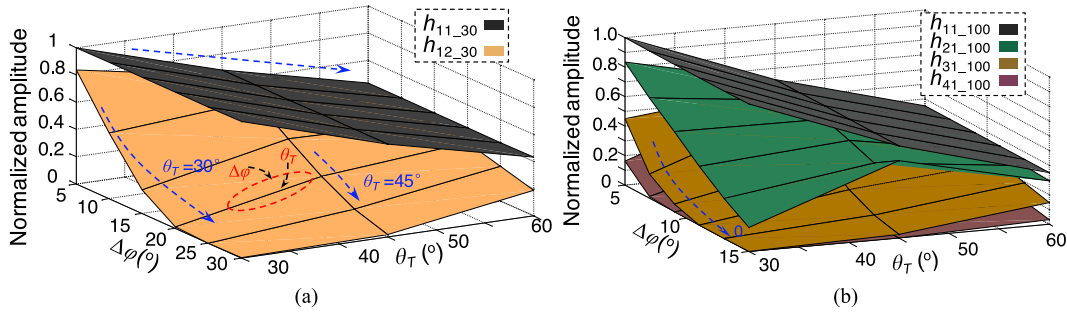
Fig. 2. (a) A three dimensional view of the 2 × 2 channel response when $r = 30$ m. The misalignment angle $\triangle\varphi$ is [5° 30°], Tx elevation angle θ_T is [30° 60°]. $\boldsymbol{H}_{2\times2}$ in all cases are normalized by the h_{11} when θ_T is 30°. (b) Channel response in 4 × 4 case when $r = 100$ m. $\boldsymbol{H}_{4\times4}$ in all cases are normalized by the h_{11} when θ_T is 30°. In our simulations, the atmospheric parameters used in the Monte Carlo channel model are as follows [6]: $\lambda = 260$ nm, $k_a = 0.802$ km^{-1}, $k_r = 0.266$ km^{-1}, $k_m = 0.284$ km^{-1}, $\gamma = 0.017$, $g = 0.72$, $f = 0.5$. (a) 2 × 2 channel response $H_{2\times2}$ at $r = 30$ m. (b) 4 × 4 channel response $H_{4\times4}$ at $r = 100$ m.
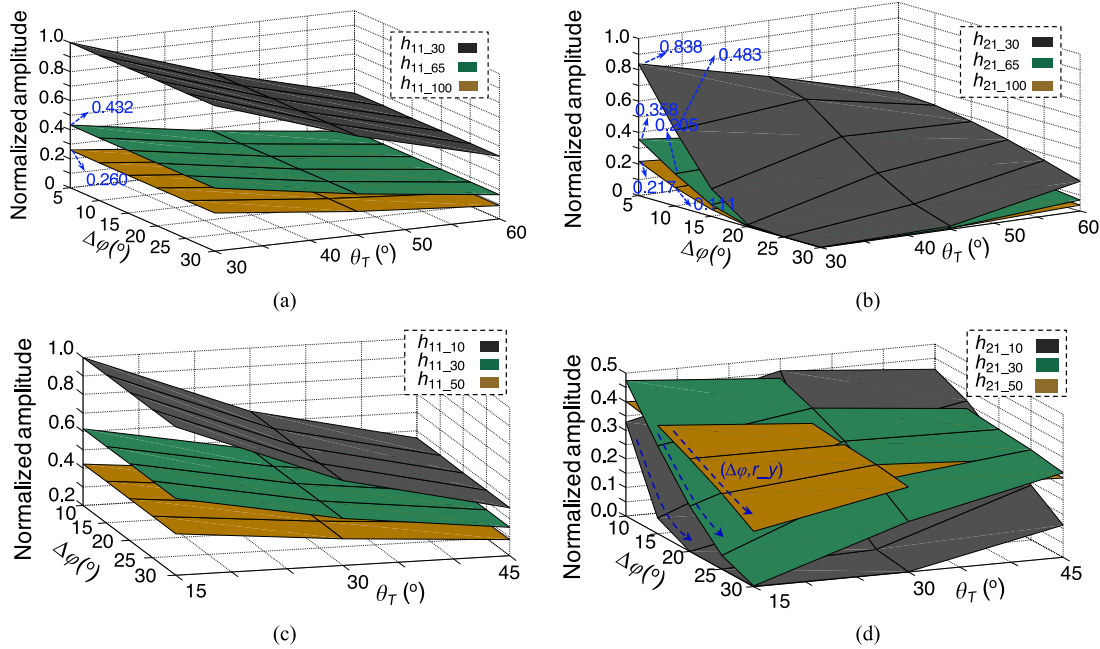

Fig. 3. 2 × 2 channel responses when nodes are moving on *x* axis and *y* axis. h_{11} and h_{21} when *x*-component movement takes place are given in (a) and (b). h_{11} and h_{21} when *y*-component movement takes place are given in (c) and (d). The distance *r* is initialized at 30 m and 65 m in two situations. r_x is selected at 35 m, 70 m. r_y is selected at 10 m, 30 m, and 50 m. (a) h_{11} of channel response $H_{2\times2}$ at $r = 30$ m, 65 m, 100 m. (b) h_{21} of channel response $H_{2\times2}$ at $r = 30$ m, 65 m, 100 m. (c) h_{11} of channel response $H_{2\times2}$ when $r = 65$ m; $r\_y = 10$ m, 30 m, 50 m. (d) h_{21} of channel response $H_{2\times2}$ when $r = 65$ m, $r\_y = 10$ m, 30 m, 50 m.

that h_{21}, h_{31}, and h_{41} approach 0 with the increase of $\triangle\varphi$. And this trend becomes more obvious as well if θ_T gets smaller. Therefore, the above channel responses confirm that proper $\triangle\varphi$ can produce fully multiplexing MIMO UV channels by this noncoplanar geometrical system structure.

Then we investigate the impacts of node mobility on the MIMO UV channel responses. Figs. 3(a) and (b) exhibit the 2 × 2 UV channel responses by *x*-component movement supposing *r* is initialized at 30 m. Here r_x is selected at 0 m, 35 m and 70 m. In other words, *r* is 30 m, 65 m and 100 m. From the results, we find that even though longer r_x leads to higher signal attenuation, the numerical

pattern of the MIMO channel response keeps steady. That is to say, the independence between subchannel elements of H is preserved when nodes are moving on x axis. As marked in Fig. 3, when θ_T is 30°, the ratios of h_{21} to h_{11} are approximately equal at different r. And this rule can also be extended to $N \times N$ cases. It should be also noted that θ_T lower than 40° is a better choice for x-component movement because wider range of $\Delta\varphi$ is able to ensure an independent MIMO UV channel responses in this case. The channel responses by y-component movement are shown in Figs. 3(c) and (d), where r is selected at 65 m, r_y is 10 m, 30 m, and 50 m. Different channel characteristics are manifested from the x-component movement. The variety of channel responses with $\Delta\varphi$ is more sensitive to r_y. From part 2.2 we know that longer r_y not only increases the transmission distance between Tx and Rx but also changes the Tx/Rx elevation angles. Consequently in y-component movement, h_{21_10} drops much faster than h_{21_30} and h_{21_50}. In addition, θ_T lower than 20° is a better choice for this situation.

3. The Modified SD Solution for Mobile MIMO UV Channels

In this section, we will firstly review the SD algorithm in part 3.1 and give the B-ary tree format of the SD for MIMO UV channels. Then based on the above symmetric MIMO UV channel characteristic, a modification is done on the SD method dependent on the QR factorization of the channel matrix. The numerical simulations are given in part 3.2. Two major objectives are destined: 1). the advantage of this geometry structure against the traditional linear array structure; 2). comparison of the BERs of the modified SD and the ZF/SD under partial correlated situations. Finally, in part 3.3, computational complexity is counted statistically to verify the feasibility of the modified SD.

3.1 Algorithm Derivation Based on the Symmetric Channel Matrix

Notations: In the derivation, we use the following notional conveniences: Given an $N \times N$ matrix P, let p_i denotes the ith column vector, p_{ii} the element in the ith row and column position, P_1^i the submatrix comprised of the first ith rows and columns. Given a vector v, let v_i denote the ith element and v_1^i the vector comprised of the first ith elements.

Theorem 2 (SD): The details of the SD method is as follows: For a MIMO UV system, several discrete time signals are involved including the transmitted symbol vector $s \in X^N$ with a finite alphabet $X = \{x_1, \ldots, x_A\}$ of size A, channel matrix H, additive noise vector n, receive vector y, and detected symbol vector $\hat{s}$ [23]. The rule of detectors is to choose the right one of the A^N possible transmitted symbol vectors. The ML detector always returns an optimal solution which uses the minimization of the squared Euclidean distance metric to target y over an N-dimensional search set $\hat{s} = \text{argmin}|y\text{-}H s|^2$, where $|y\text{-}H s|^2$ is called objective function [24]. Based on the enumeration of points in the search set that are located with a sphere of some radius centered at one of the targeted receive symbols, SD method can reduce the extremely huge search times of the ML. The underlying principle of the SD is the QR factorization of $H = QR$, where Q is orthogonal, R is upper triangular and invertible [25]. Thus the above minimization problem can be written as $\text{argmin}|\hat{y}\text{-}Rs|^2$, where $\hat{y} = Q^T y$ is an orthogonal transformation of the original receive vector y. In this way, the upper triangular feature of R enables the detector to decompose the objective function into summations as follows

$$\left|\hat{y} - Rs\right|^2 = d^2(\hat{y}_N, r_{NN}s_N) + \left|(\hat{y} - r_N s_N)_1^{N-1} - R_1^{N-1}s_1^{N-1}\right|^2$$

$$= \sum_{i=N}^{1} d(\hat{u}(s_{i+1})_i, r_{ii}s_i), \tag{4}$$

where $d^2(\cdot)$ is the squared Euclidean distance and $\hat{u}(s_{i+1}) = \hat{y}\text{-}r_{i+1}s_{i+1}$ ($r_{N+1} = 0$, $s_{N+1} = 0$).

Proof 1 (B-ary Tree): In MIMO UV systems, the spatial transmitted symbol in a temporal timeslot from each Tx is a bit-1 or bit-0 pulse for both PPM and OOK modulations [7]. Then, the above $X = \{x_1, \ldots, x_A\}$ can be simplified as $X = \{0, 1\}$. If so, The Eq. (4) naturally lends the SD of MIMO
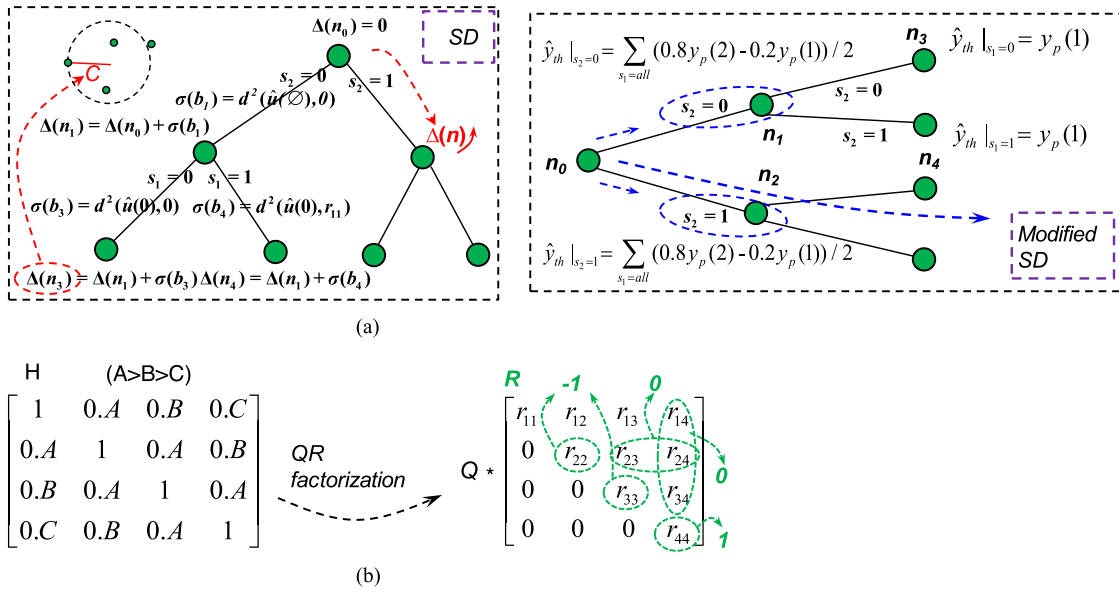
Fig. 4. Illustration of the SD algorithm and the modification based on the symmetric MIMO UV channel matrix characteristics by QR factorization. (a) Algorithm principle. (b) Symmetric channel QR factorization.

UV channels to a *B*-ary tree format as shown by a 2×2 case example in Fig. 4 (a). In the diagram, every term in Eq. (4) is associated with a branch s_i and the summation in Eq. (4) is equal to the weight of the leaf nodes. From the tree, we observe that the search operation is traversed in order from s_N to s_1 because of the upper triangular feature of $\boldsymbol{R}$.

Since the node weights are non-decreasing along the paths from the root to leaf nodes, SD can reduce the search of ML solution to polynomial number by pruning the tree by intermediate node weights. As shown in Fig. 4(a), given a radius C, only leaf nodes will be explored with weights within C. However, the SD search is high dependent on the selection of C and the program realization of the SD solution is complicated. In order to achieve a linear computational complexity and a simple implementation, we revise the search strategy in SD by the threshold direct detection in each branch of the B-ary tree as shown in the right part of Fig. 4(a).

Proof 2 (numerical pattern of $\boldsymbol{R}$): The modified SD also relies on the QR factorization of $\boldsymbol{H}$. The idea of this modification is contributed from the symmetric MIMO UV channel matrix H. Fig. 4(b) provides an interpretation of the unique behavior of $\boldsymbol{H}$ in 4×4 example after QR factorization. By conducting the QR factorization on the real symmetric matrix $\boldsymbol{H}$, the absolute diagonal members of $\boldsymbol{R}$ are approximate to 1, while the others are close to 0 if H is closer to an identity matrix owing to stronger channel independence by larger $\Delta \varphi$. Numerical results are given in Fig. 5 to prove this phenomena. The subchannel elements of $\boldsymbol{R}$ under various $\Delta \varphi$ in 2×2 and 4×4 cases when $r = 100$ m, $\theta_T = 30°$ are given in Fig. 5(a) and (b).

Theorem 3 (modified SD): The algorithm procedure of the modified SD in is illustrated in Fig. 4(a). The detection is also carried on in order from s_N to s_1. Assuming s_N is on the detection queue, $\hat{y}_N$ will be closer to 1 if $s_N = 1$ for the numerical feature of $\boldsymbol{R}$ mentioned above. On the other hand, $\hat{y}_N$ is closer to 0 if $s_N = 0$. Thus the priori value of s_N ($\hat{s}_N$) primarily depends on $\hat{y}_N$. As shown by Fig. 4 (a), through allocate a heavy weight w to $\hat{y}_N$ and a light weight w_other to the summation of $\hat{y}_1$ to $\hat{y}_{N-1}$ ($w = 0.8$, $w\_other = 0.2$ in our simulations), we could obtain a threshold $\hat{y}_{th}(s_N = 0|1)$ to decide whether s_N is 0 or 1 by counting the average difference between the weighted $\hat{y}_N$ and the weighted summation of $\hat{y}_1$ to $\hat{y}_{N-1}$ in all cases when $s_N = 0$ or 1. This threshold can be applied to all the branches connected with the leaf nodes n_i ($i = 1, .., 2^N$) in the tree. Let $\boldsymbol{y_p} = \boldsymbol{R} \cdot [s_1 \dots s_n]$ ($s_n = 1|0$, $s_{1 \sim n-1} \in \{0, 1\}$) denote the vector space, the threshold $\hat{y}_{th}(s_n = 0|1)$ is
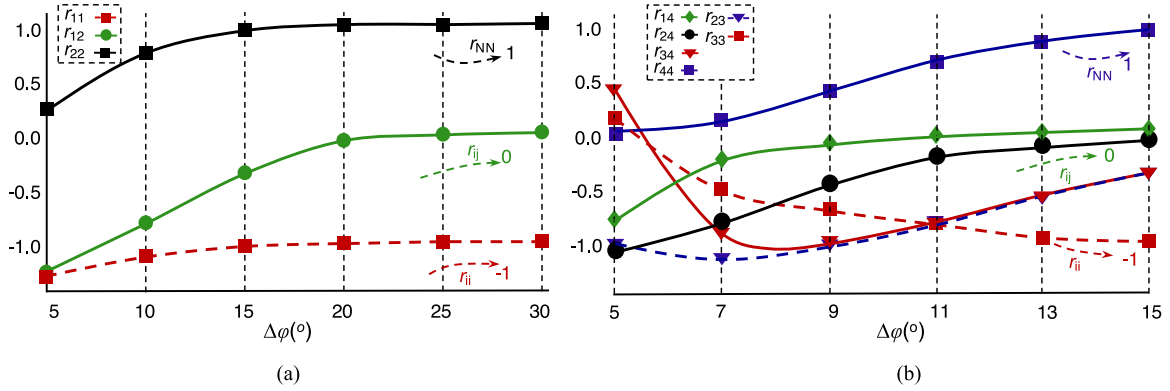
Fig. 5. Demonstration of the numerical pattern of R in 2×2 and 4×4 cases. (a) R of 2×2 channel matrix when $r = 100$ m, $\theta_T = 30°$. (b) R of 4×4 channel matrix when $r = 100$ m, $\theta_T = 30°$.

expressed as

$$\hat{y}_{th}(s_n = 0|1) = \sum_{s_{1\sim n-1}=all} (wy_p(n) - w\_other \sum_{i=1}^{n-1} y_p(i))/2^{n-1}. \quad (5)$$

Initializing n with N and $n = n - 1$ in each step, the algorithm is ended by repeating the threshold detection recursively to the last leaf node. Note that in each step, $y_p = y_p - r_n s_n$ to eliminate the impact of current detected symbol to the next one. Thus the whole detection process only consumes N times of searches just like the simplified ZF detection because each symbol in the symbol vector s can be straightly detected by the threshold.

3.2 Numerical Results of the BER Performance and Discussions

At first, to verify the above the noncoplanar geometrical MIMO structure design and modified SD solution, we evaluate the system BERs in 4×4 cases when $\theta_T = 30°$ and $r = 100$ m, where the information bits are encapsulated in each packet of size 10000. Fig. 6 gives a fair comparison of the BERs of the noncoplanar geometry and traditional linear array structure. Meanwhile the BERs using the ZF, SD and modified SD when $\triangle \varphi = 10°$ are also presented. Because the UV link performance is changing with different r and θ_T, the SNR is used to evaluate the system BER performance for analysis convenient. The SNR at the receiver side ranges from 0 to 20 dB in our simulation.

The results convince that the noncoplanar MIMO UV system geometry works well as expected from the channel responses in Section 2.3. $\triangle \varphi$ is quite significant for the MIMO detection accuracy because the independence between subchannel elements in the channel matrix is strengthened with larger $\triangle \varphi$ as mentioned before. Fully multiplexing is ensured when $\triangle \varphi > 17°$ by this noncoplanar MIMO geometry. In fully multiplexing conditions, each subchannel can be treated like a single link where the received signal sequences are detected without inter-subchannel interference. In this case, the BER below 10^{-3} can be reached easily and the data rate will be lifted up to fourfold of a single link without extra BER performance loss. On the contrary, difficulty and inconvenience occurs in the traditional linear array structure. The BERs of the linear array MIMO systems when $d_u = 2$ m, 5 m, 10 m are illustrated in Fig. 6. From the results, we find that channel independence is relatively hard to promise in linear array structure due to the UV scattered propagation. The size of the MIMO transceiver D_S will be very large if the linear array structure is used to generate a multiplexing MIMO UV channel. While D_S remains 0 m in the noncoplanar MIMO geometry as the noncoplanar misalign angle is employed to overcome the spatial correlation.

Furthermore, the practical limitations or large numbers of antenna in the noncoplanar geometrical coordinate may produce an inadequate misalign angle $\triangle \varphi$. As described above, MIMO detections
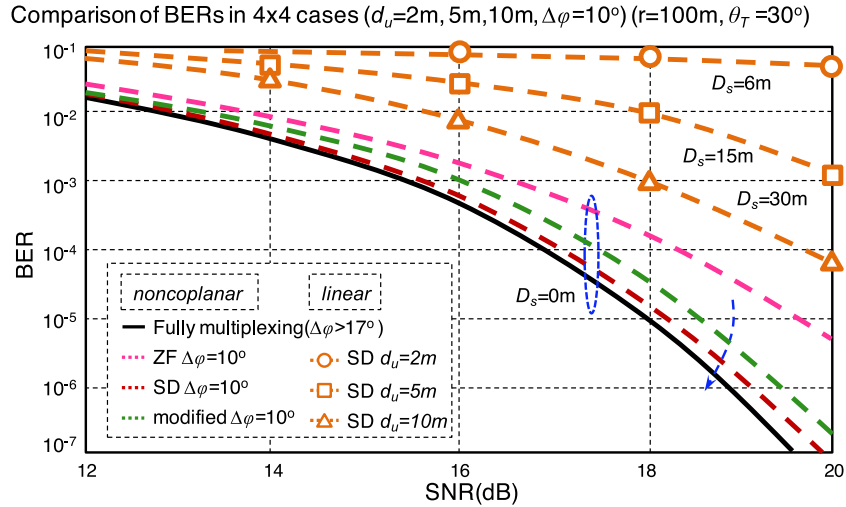
Fig. 6. Comparison of BERs of the noncoplanar MIMO geometry and the traditional linear array MIMO structure. In the simulations, $r = 100$ m, $\theta_T = 30°$. Fully multiplexing is enabled when $\triangle\varphi > 17°$ by the noncoplanar geometry. Comparison of the BERs using ZF, SD and modified SD when $\triangle\varphi = 10°$ is also done to verify the feasibility of the modified SD.
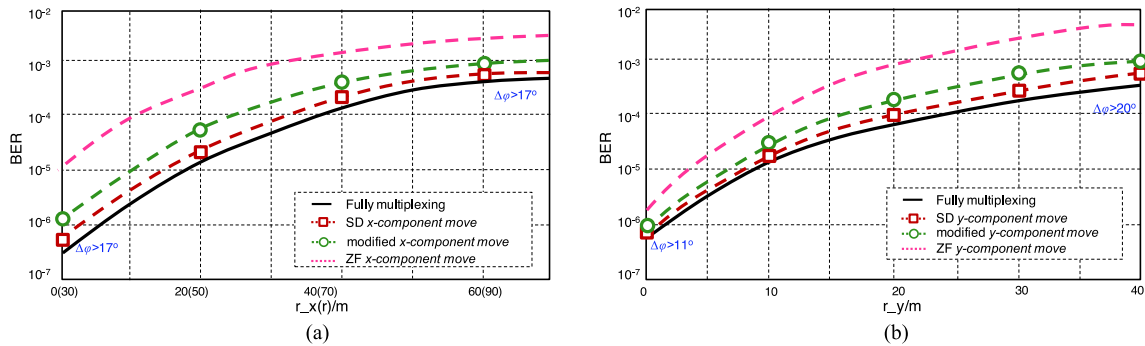

Fig. 7. Comparison of BERs using the ZF, SD and modified SD in mobile MIMO UV channels. In x-component movement, $\theta_T = 30°$, SNR is supposed to 16 dB at $r = 100$ m. In y-component movement, $\theta_T = 15°$, SNR is supposed to 18 dB at $r\_y = 40$ m. (a) BERs of x-component movement ($\theta_T = 30°$, $\triangle\varphi = 10°$ SNR $= 16$ dB ($r = 100$ m)). (b) BERs of y-component movement ($\triangle\varphi = 10°$, $\theta_T = 15°$, SNR $= 18$ dB($r\_y = 40$ m, $r = 65$ m)).

are developed to cut the inter-subchannel interference brought by the partial spatial correlation. Thus we investigate the MIMO detections based on the channel model. The BERs of the ZF, SD and modified SD when $\triangle\varphi = 10°$ are also plotted in Fig. 6. It is observed that except the linear computational complexity, the BER performance of the modified SD is much better than the ZF. About 5~10 dB BER gains are achieved by the modified SD over ZF. Meanwhile, the orders of the BERs by the modified SD and SD are always consistent. Even though $\triangle\varphi$ is lower than 17°, the BERs of the SD and modified SD are still close to the fully multiplexing conditions. Thereby, the above results prove that the geometrically noncoplanar MIMO UV system design is able to create near fully multiplexing MIMO UV channels even if when partial spatial correlation exists and the modified SD method is effective for the symmetric MIMO UV channel.

Continuing with the previous discussions, we further investigate the noncoplanar geometry and the modified SD in mobile scenarios as shown in Fig. 7 to explore the impacts of node mobility on the BER performance. In our simulations, r is initialed at 30 m and r_x is selected at 0 m, 20 m, 40 m, 60 m in x-component movement, r is 65 m and r_y is selected at 0 m, 10 m, 20 m, 30 m, and 40 m in y-component movement.
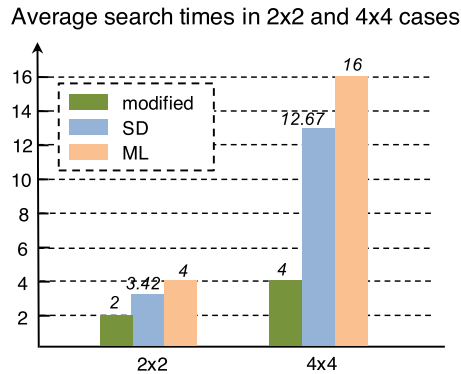
Average search times in 2x2 and 4x4 cases

Fig. 8. Statistical counting of search times of ML, SD and modified SD.

Fig. 7(a) shows the BERs in *x*-component movement, where $\theta_T = 30°$, SNR is supposed to 16 dB at $r = 100$ m. From the results, it is observed the order of BER by the modified SD solution is consistent with the SD as well in mobile MIMO UV channels. BER lower than 10^{-3} can also be achieved by the modified SD when $\Delta\varphi$ is larger than 10°. As *x*-component movement does not change the subchannel independence of the MIMO UV channel as mentioned before. $\Delta\varphi$ has a limited influence on the system performance in *x*-component movement. Thus, in this case, $\Delta\varphi > 17°$ can satisfy the fully multiplexing condition with the increase of r_x.

Next we turn to *y*-component movement situations. Because the Tx elevation angles relative to the initial value is lifted by *y*-component movement which defects the subchannel independence besides the path loss, we selected the θ_T as 15° when $r\_y = 0$ m. Fig. 7(b) shows the numerical results, where SNR is supposed to 18 dB at $r\_y = 40$ m. From the results, we find that *y*-component movement affects the BER differently from the *x*-component movement. The BER curves rise faster with r_y compared with r_x. Nevertheless, fully multiplexing can be provided by this noncoplanar geometry in *y*-component movement. Due to the Tx elevation angle variety induced by *y*-component movement, the $\Delta\varphi$ enabling the fully multiplexing channel rises from 12° to 20° when r_y increase from 0 m to 40 m. Similar to *x*-component, the modified SD outperforms ZF and the order of BER is consistent with the SD when $\Delta\varphi = 10°$. In addition, as channel independence is weaken by longer r_y, the difference between the BER of fully multiplexing condition and when $\Delta\varphi = 10°$ gets a little higher with longer r_y.

3.3 Comparison of the Computational Complexity

Finally, the total search times are statistically counted for the ML, SD and modified SD as shown in Fig. 8. An average amount of 3.42 and 12.67 are counted for the SD in 2×2 and 4×4 cases. Hence the computational complexity of SD can be analytically fitted by a polynomial function $n^{1.841}$-0.165. Whereas, the computational complexity function of the ZF/modified SD and ML can be directly modeled as n and 2^n. Therefore, it is clear that the modified SD solution for MIMO UV signal detection achieves a huge improvement of computational complexity for by sacrificing tiny BER performance loss.

4. Conclusion

In conclusions, mobile MIMO UV channel models and a low-complexity MIMO detection method are introduced simultaneously into the NLOS UV communication. We put forward a kind of UV mesh network framework and consider the UV channel mobility in the mesh grid structure. Then in order to satisfy the high rate requirements of a mobile network, multiplexing MIMO UV system is focused on in this paper. A noncoplanar MIMO UV system design is proposed geometrically-based. Spatially independent MIMO UV channels are resulted by this special geometry. Large datasets of

the MIMO UV channel response are collected in the mobile mesh network model. Following the algorithm diagram of the typical sphere decoding (SD) method, we develop a modified SD method to reduce computational complexity from polynomial to linear. Furthermore, BER performance of the modified SD is evaluated exhaustively in mobile MIMO UV channels under various geometric parameters. Results show that the noncoplanar MIMO UV system is very effective and the order of BERs using the modified SD is always consistent with the SD in all cases.

Acknowledgment

References

[1] P. Daukantas, "Optical wireless communications: The new "Hot Spots"?" *Opt. Photonics News*, vol. 25, no. 3, pp. 34–41, 2014.
[2] G. Chen, F. Abou-Galala, Z. Xu, and B. M. Sadler, "Experimental evaluation of LED-based solar blind NLOS communication links," *Opt. Exp.*, vol. 16, no. 19, pp. 15059–15068, 2008.
[3] H. Zhang, H. Yin, H. Jia, J. Yang, and S. Chang, "Study of effects of obstacle on non-line-of-sight ultraviolet communication links," *Opt. Exp.*, vol. 19, no. 22, pp. 21216–21226, 2011.
[4] Z. Xu and B. M. Sadler, "Ultraviolet communications: Potential and state-of-the-Art," *IEEE Commun. Mag.*, vol. 46, no. 5, pp. 67–73, May 2008.
[5] Z. Xu, "Opportunities and challenges in ultraviolet communications," in *Proc. IEEE Summer Topicals Meet. Series*, 2015, pp. 171–172.
[6] H. Ding, G. Chen, A. Majumbar, B. M. Sadler, and Z. Xu, "Modeling of non-line-of-sight ultraviolet scattering channels for communication," *IEEE J. Sel. Areas Commun.*, vol. 27, no. 9, pp. 1535–1544, Dec. 2009.
[7] P. Luo, M. Zhang, D. Han, and Q. Li, "Performance analysis of short-range NLOS UV communication system using Monte Carlo simulation based on measured channel parameters," *Opt. Exp.*, vol. 20, no. 21, pp. 23489–23501, 2012.
[8] Q. He, Z. Xu, and B. M. Sadler, "Performance of short-range non-line-of-sight LED-based ultraviolet communication receivers," *Opt. Exp.*, vol. 18, no. 12, pp. 12226–12238, 2010.
[9] X. Zhang, Y. Tang, H. Huang, L. Zhang, and T. Bai, "Design of an omnidirectional optical antenna for ultraviolet communication," *Appl. Opt.*, vol. 53, no. 15, pp. 3225–3232, 2014.
[10] A. Vavoulas, H. G. Sandalidis, and D. Varoutas, "Connectivity issues for ultraviolet UV-C networks," *J. Opt. Commun. Netw.*, vol. 3, no. 3, pp. 199–205, 2011.
[11] A. Vavoulas, H. G. Sandalidis, and D. Varoutas, "Node isolation probability for serial ultraviolet UV-C multi-hop Networks," *J. Opt. Commun. Netw.*, vol. 3, no. 9, pp. 750–757, 2011.
[12] T. Zhao, Y. Gao, and Y. Zhang, "An area coverage algorithm for non-line-of-sight ultraviolet communication network," *Photonic Netw. Commun.*, vol. 32, no. 2, pp. 269–280, 2016.
[13] I. F. Akyidiz, "Wireless mesh network: A survey," *Comput. Netw.*, vol. 4, no. 4, pp. 445–487, 2005.
[14] G. Chen, Z. Xu, and B. M. Sadler, "Experimental of ultraviolet pulse broadening in short-range non-line-of-sight communication channels," *Opt. Exp.*, vol. 18, no. 10, pp. 10500–10509, 2010.
[15] M. Zhang *et al.*, "Spread spectrum-based ultraviolet communication with experiments," *Chin. Opt. Lett.*, vol. 12, no. 10, pp. 100602–100608, 2014.
[16] M. A. El-Shimy and S. Hranilovic, "Binary-Input non-line-of-sight solar-blind UV channels: Modeling, capacity and coding," *J. Opt. Commun. Netw.*, vol. 4, no. 12, pp. 1008–1017, 2012.
[17] H. Qin, Y. Zuo, D. Zhang, Y. Li, and J. Wu, "Received response based heuristic LDPC code for short-range non-line-of-sight ultraviolet communication," *Opt. Exp.*, vol. 25, no. 5, pp. 5018–5030, 2017.
[18] C. Wang, F. Haider, X. Gao, and X. You, "Cellular architecture and key technologies for 5G wireless communication networks," *IEEE Commun. Mag.*, vol. 52, no. 2, pp. 122–130, Feb. 2014.
[19] D. Han, Y. Liu, K. Zhang, P. Luo, and M. Zhang, "Theoretical and experimental research on diversity reception technology in NLOS UV communication system," *Opt. Exp.*, vol. 20, no. 14, pp. 15833–15842, 2012.
[20] G. Chen and Z. Xu, "LMMSE SIMO receiver for short-range non-line-of-sight scattering communication," *IEEE Trans. Wireless Commun.*, vol. 14, no. 10, pp. 5338–5349, Oct. 2015.
[21] M. A. El-Shimy and S. Hranilovic, "Spatial-diversity imaging receivers for non-line-of-sight solar-blind UV communications," *J. Lightw. Technol.*, vol. 33, no. 11, pp. 2246–2255, Oct. 2015.
[22] A. J. Paulraj, D. A. Gore, R. U. Nabar, and H. Bolcskei, "An overview of MIMO communications-A key to gigabit wireless," *Proc. IEEE*, vol. 92, no. 2, pp. 198–218, Feb. 2004.
[23] G. Huang, Y. Tang, G. Ni, H. Huang, and X. Zhang, "Application of MIMO technology in ultraviolet communication," *Proc. SPIE*, vol. 9043, pp. 237–244, 2013.
[24] K. Su, *Efficient Maximum Likelihood Detection for Communication Over Multiple Input Multiple Output Channels*. Cambridge, U.K.:Univ. of Cambridge, 2005.
[25] Z. Guo and P. Nilsson, "Algorithm and implementation of the K-best sphere decoding for MIMO detection," *IEEE J. Sel. Areas Commun.*, vol. 24, no. 24, pp. 491–503, Mar. 2006.
[26] M. Mansuripur, *Classical Optics and its Applications*. Cambridge, U.K.: Cambridge Univ. Press, 2009.
[27] H. Xiao, Y. Zuo, J. Wu, H. Guo, and J. Lin, "Non-line-of-sight ultraviolet single-scatter propagation model," *Opt. Exp.*, vol. 19, no. 18, pp. 17864–17875, 2011.